frontiers in Chemistry

ORIGINAL RESEARCH
published: 21 February 2020
doi: 10.3389/fchem.2020.00096

Fabrication of SiO_x-G/PAA-PANi/Graphene Composite With Special Cross-Doped Conductive Hydrogels as Anode Materials for Lithium Ion Batteries

Yuanhong Liao[1], *Kang Liang*[1], *Yurong Ren*[1]* *and Xiaobing Huang*[2]

[1] School of Materials Science and Engineering, Jiangsu Collaborative Innovation Center of Photovoltaic Science and Engineering, Changzhou University, Changzhou, China, [2] Hunan Province Cooperative Innovation Center for the Construction & Development of Dongting Lake Ecological Economic Zone, College of Chemistry and Materials Engineering, Hunan University of Arts and Science, Changde, China

Silicon oxides (SiO_x) have been considered to be the likeliest material to substitute graphite anode for lithium-ion batteries (LIBs) due to its high theoretical capacity, appropriate working potential plus rich abundance. Nevertheless, the two inherent disadvantages of volume expansion and low electrical conductivity of SiO_x have been a main obstacle to its application. Here, SiO_x-G/PAA-PANi/graphene composite has been successfully synthesized by *in-situ* polymerization, in which SiO_x-G particles linked together by a graphene-doped polyacrylic acid-polyaniline conductive flexible hydrogel and SiO_x-G is encapsulated inside the conductive hydrogel. We demonstrate that SiO_x-G/PAA-PANi/graphene composite possesses a discharge-specific capacity of 842.3 mA h g^{-1} at a current density of 500 mA g^{-1} after a cycle life of 100 cycles, and a good initial coulombic efficiency (ICE) of 74.77%. The superior performance probably due to the lithium ion transmission rate and the electric conductivity enhanced by the three-dimensional (3D) structured conductive polymer hydrogel.

Keywords: lithium-ion batteries, anode material, SiO_x, PAA-PANi, graphene, conductive hydrogel

OPEN ACCESS

Edited by:
Zhangxing He,
North China University of Science and Technology, China

Reviewed by:
Mingyong Wang,
University of Science and Technology Beijing, China
Xifei Li,
Xi'an University of Technology, China

***Correspondence:**
Yurong Ren
ryrchem@163.com

Specialty section:
This article was submitted to Electrochemistry, a section of the journal Frontiers in Chemistry

Received: *29 October 2019*
Accepted: *31 January 2020*
Published: *21 February 2020*

Citation:
Liao Y, Liang K, Ren Y and Huang X (2020) Fabrication of SiO_x-G/PAA-PANi/Graphene Composite With Special Cross-Doped Conductive Hydrogels as Anode Materials for Lithium Ion Batteries. Front. Chem. 8:96. doi: 10.3389/fchem.2020.00096

INTRODUCTION

Lithium-ion batteries (LIBs), presumably among the most prospective devices for energy storage, are featured with higher energy density, longer cycle life, lower self-discharging, and more safety. Developing advanced LIBs with highly advanced energy density and cyclability is an immediate need for lightweight electronics and range expansion of electric vehicles. Yet the current graphite anode with an unsatisfactory specific capacity of ~372 mA h g^{-1} (LiC_6) can't follow the development of modern equipment for high energy storage system (Casimir et al., 2016; Zuo et al., 2017; Han et al., 2018; Yi et al., 2018, 2019; Zheng et al., 2018, 2020; Xiao et al., 2019). Hence, silicon has become a potential candidate to replace commercial graphite anode for LIBs in that it has higher capacity (~4,200 mA h g^{-1}), suitable discharge platform (~0.4 V vs. Li/Li^+) and sufficient resources (Casimir et al., 2016; Jiang et al., 2016; Xu et al., 2018; An et al., 2019; Liu Y. et al., 2019a; Yang et al., 2019; Zhou et al., 2019; Zuo et al., 2019). Nevertheless, the two stubborn disadvantages of silicon,

including the deterioration of electrode structure integrity as a result of gradual enhancement of pulverization happening in the repetition of discharge/charge process, as well as poor conductivity, have been the main obstacles to its application (Zhao et al., 2016; Zuo et al., 2017). To address the above-mentioned key issues, a series of countermeasures have been taken, such as optimizing structure, doping and coating with carbon or other conductive materials.

Compared with Si-based materials, SiO_x-based anodes are prone to achieve remarkable electrochemical performance due to the formation of Li_2O and Li silicates, which can form the stable solid electrolyte interphase (SEI) layer and adapt to the volume expansion of SiO_x during the insertion of Li^+ (Nguyen et al., 2013; Xu et al., 2017; Liu D. et al., 2019; Liu Y. et al., 2019b; Zheng et al., 2019). Although the capacity of SiO_x is high, the volume multiplication usually causes this material to crack and pulverize. Besides, the low intrinsic conductivity of SiO_x would lead to poor rate performance (Xu et al., 2017; Xiao et al., 2018; Fang et al., 2019; Li et al., 2019; Wang et al., 2020). Different ways have been adopted to overcome these issues, including doping the host framework with conductive particle, coating the electrodes with buffer materials, bettering the morphology, cutting the size of dimension and applying more effective binders. For example, Yu et al. obtained the pomegranate-liked nano-scale SiO_x-C by spray drying, the prepared composite presents a discharge specific capacity of 1,024 mA h g^{-1} when the current density is 500 mA g^{-1} after 200 cycles (Yu et al., 2018). Jiang et al. taken advantage of graphene bubbles to encapsulate the SiO_x inside to accelerate ion transmission rate of the material, achieving 80% capacity retention after 1,000 cycles (Jiang et al., 2016).

Conducting polymers (CPs), such as polyaniline (PANi), polyacetylene, polythiophene (PTh), Polypyrrole (PPy), and et al., providing special 3D network nanostructures and high conductivity as a result of their large conjugated π bonds structure (Li et al., 2009; Li J. et al., 2018; Li P. et al., 2018). At the same time, CPs have been verified as significant materials for the advancement of modern society, consisting of energy storage, semiconductor sensors and catalysis. For example, a PANi/CNT composite electrode synthesized via the way of *in-situ* chemical polymerization of aniline in a well-dispersed CNT solution revealed excellent electrochemical behavior. As the cathode material for LIBs, the PANi/CNT possessed a high energy density of 86 mA h g^{-1} at the 80th cycle and an average coulombic efficiency of 98% (Li et al., 2009). Also, SiO_x-PANi–Ag composite electrodes were synthesized by Zhang et al. via *in-situ* polymerization, and exhibited great cycling performances (with a reversible capacity of 1,149 mA h g^{-1} after 100 cycles) (Wang et al., 2014). Wu et al. prepared SiNP-PANi with a capacity retention rate of more than 90% after 5,000 cycles at a current density of 6.0 A g^{-1} (Wu et al., 2013).

Besides, the carbon bonds of graphene are sp2 hybridized, exhibiting a number of intriguing and unique properties such as high surface area, admirable electronic conductivity and superior mechanical properties (Huang et al., 2011; Li P. et al., 2018). It is very meaningful that the properties make graphene-based materials useful for modifying silicon-based materials (Jiang et al., 2016). For example, Zhu et al. constructed Si@SiO_x/GH composite with a stable storage capacity of 1,020 mA h g^{-1} at 4 A g^{-1} (Zhu et al., 2019).

Herein, we provide a flexible and harmless method for synthesizing SiO_x-G/PAA-PANi/graphene (**Scheme 1**). Firstly, SiO_x-G was synthesized by a method of high-energy mechanical ball milling (Jiang et al., 2016). Then, Polyacrylic acid and Polyaniline are doped with each other by *in-situ* polymerization as a framework to synthesize SiO_x-G/PAA-PANi. Finally, the graphene dispersion is added to obtain the SiO_x-G/PAA-PANi/graphene. This intertwined doping not only can provide a continuous path for electron conduction, but also stabilize the material structure. Hence, the SiO_x-G/PAA-PANi/graphene exhibits superior electrochemical performance.

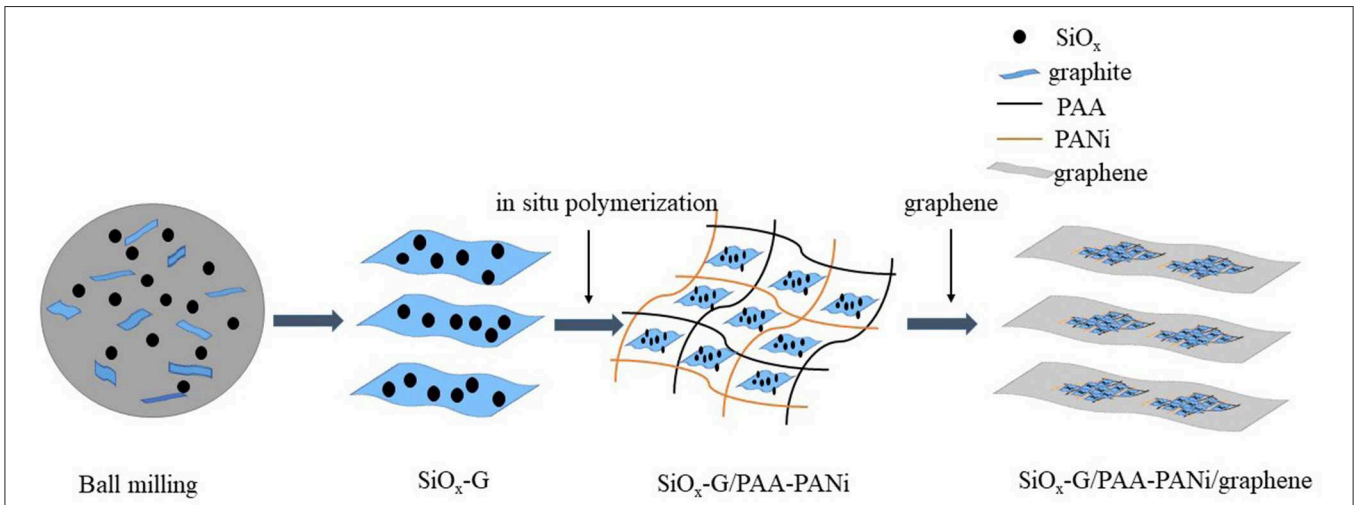

SCHEME 1 | Schematic illustration for preparation of SiO_x-G/PAA-PANi/graphene composites.

EXPERIMENTAL

Material Preparation

Synthesis of SiO_x-G

SiO_x-G was obtained by a solid state method. Firstly, SiO_x is prepared by ball milling (QM-3SP4, Nanjing, China) SiO in Ar for 6 h (500 rpm, the ball-to-particulate weight ratio of 30:1). Secondly, 6.0 g of Graphite was heated at 600°C for 20 min in Ar flow and then mixed with 6.0 g of SiO_x by ball milling for 6 h under the same ball milling conditions as the process for preparation of SiO_x. The above composite material is recorded as SiO_x-G.

Synthesis of SiO_x-G/PAA-PANi

Firstly, 0.005 g of PAA was weighed and dissolved in a 25 ml beaker and placed in an oven at 60°C for 1 h, and then an appropriate amount of 0.5 M NaOH was added. Secondly, 0.2 g of SiO_x-G was dissolved in the above sodium polyacrylate solution, and ultrasonicated for 1 h, followed by stirring in an ice bath (Li P. et al., 2018). Subsequently, aniline and $(NH_4)_2S_2O_8$ were added and stirred for 40 min. The target production was obtained after standing, dialysis, and lyophilization.

Synthesis of SiO_x-G/PAA-PANi/Graphene

The preparation steps are the same as the synthesis process of SiO_x-G/PAA-PANi, except that the dispersion of 0.002 g of graphene is stirred for 1 h before standing. The obtained sample was named as SiO_x-G/PAA-PANi/graphene.

Material Characterization

The as-prepared product was characteristic of X-ray diffraction (XRD, D/max 2500 PC) with the use of Cu Ka radiation. X-ray photoelectron spectroscopy (XPS) data was recorded by the Electronic detection system (Thermo VG Scientific ESCA Lab 250). Thermogravimetric analysis (TGA) data is recorded from indoor temperature to 800°C at a rate of 10°C min^{-1} under an oxygen atmosphere. The data analysis of Fourier transform infrared (FT-IR) spectroscopy was undertaken by an IR spectrophotometer (Thermo Fisher, American). The morphology and element distribution are presented by high-resolution field emission scanning electron microscopy (FESEM, Zeiss, Germany). Transmission electron microscopy (TEM) were performed on a JEOL 2100 worked at 200 kV.

Electrochemical Measurements

In preparation for the working electrode, the active material (75%), the conductive agent (Acetylene black,10%) and the binder (Sodium alginate,15%) were uniformly mixed to obtain the slurry, and coated on the upper part of the current collector (copper foil) and placed in a vacuum oven at 105°C for 8 h. CR2032-type coin half-cell was converged in a glove box filled with high purity argon (O_2 and H_2O < 0.5 ppm), with 1 M $LiPF_6$ dissolved in ethylene carbonate: dimethyl carbonate: ethyl methyl

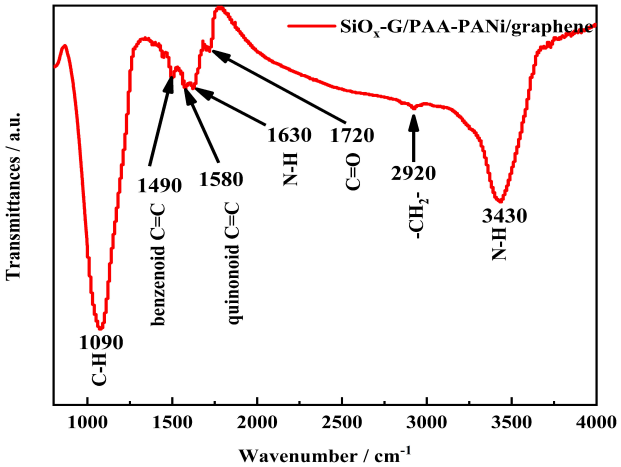

FIGURE 2 | FT-IR image of SiO_x-G/PAA-PANi/graphene.

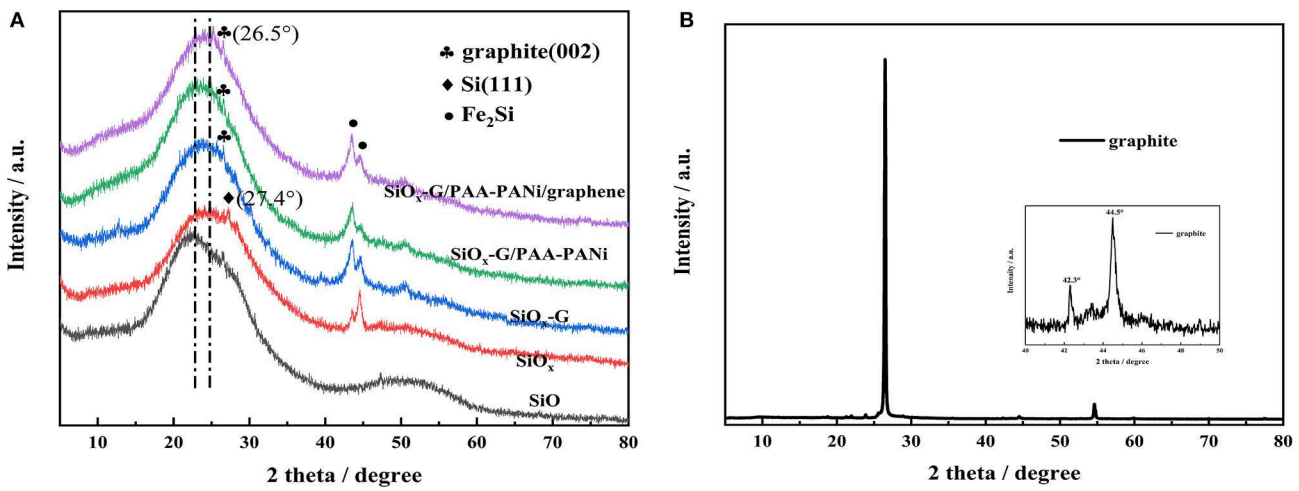

FIGURE 1 | (A) XRD image of SiO, SiO_x, SiO_x-G, SiO_x-G/PAA-PANi, and SiO_x-G/PAA-PANi/graphene; **(B)** XRD image of graphite.

carbonate (1:1:1 in volume), and 10% of fluorinated ethylene carbonate was further added as the electrolyte, Celgard 2500 film as the separator, and lithium foil as the counter electrode. The cyclic stability test and rate performance test of the material can be achieved on Land-CT 2001A instrument where the potential is 0.01 V−3 V and the current density is 500 mA g^{-1} at 25°C. Cyclic Voltammetry (CV) was recorded by electrochemical analyzer (CHI 604E, Chen He Instruments, Shanghai).

RESULTS AND DISCUSSION

XRD patterns of four samples were compared in **Figure 1A**. As illustrated, commercial silicon monoxide is amorphous, which is consistent with previous findings (Hwa et al., 2013; Yu et al., 2013). Compared with SiO, the position of the broad peak of SiO_x shifted from 22° to 24.8°. Also, it is observed that there is a distinct characteristic peak of Si (111) located at 27.2° in as-obtained SiO_x sample, which might be due to that a part of SiO is reduced to Si after ball milling (Jiang et al., 2016). In addition, two peaks at 43.4° and 44.5° were observed in SiO_x samples, corresponding to the characteristic peak of Fe_2Si, which might be created from the stainless steel ball and Si during the process of ball milling. Similar phenomenon was also demonstrated by Qian et al. (2017). **Figure 1B** shows the XRD pattern of graphite. The crystal plane characteristic peak of graphite (002) is situated at 26.5° in SiO_x-G, SiO_x-G/PAA-PANi and SiO_x-G/PAA-PANi/graphene samples (**Figure 1A**), showing that the existence of graphite in the three samples.

Fourier transform infrared (FT-IR) spectrum of SiO_x-G/PAA-PANi/graphene is shown in **Figure 2**. The absorption peaks at 3,430 and 2,920 cm^{-1} correspond to the N-H bending vibration absorption peak and -CH_2- stretching vibration absorption peak, respectively. In addition, the bands at 1,720 and 1,090 cm^{-1} are attributed to C=O bending vibration and C-H bending vibration. The presence of above several absorption peaks are sufficient to prove the existence of PAA (Wang et al., 2015). The weaker absorption peak from 1,400 to

TABLE 1 | The proportion of different valence states of Si in SiO_x-G/PAA-PANi/graphene.

Production	Si^0	Si^{+1}	Si^{+2}	Si^{+3}	Si^{+4}
Position/eV	99.98	102.06	102.85	103.68	105.00
Percentage/%	15.55	20.11	29.63	29.63	5.08

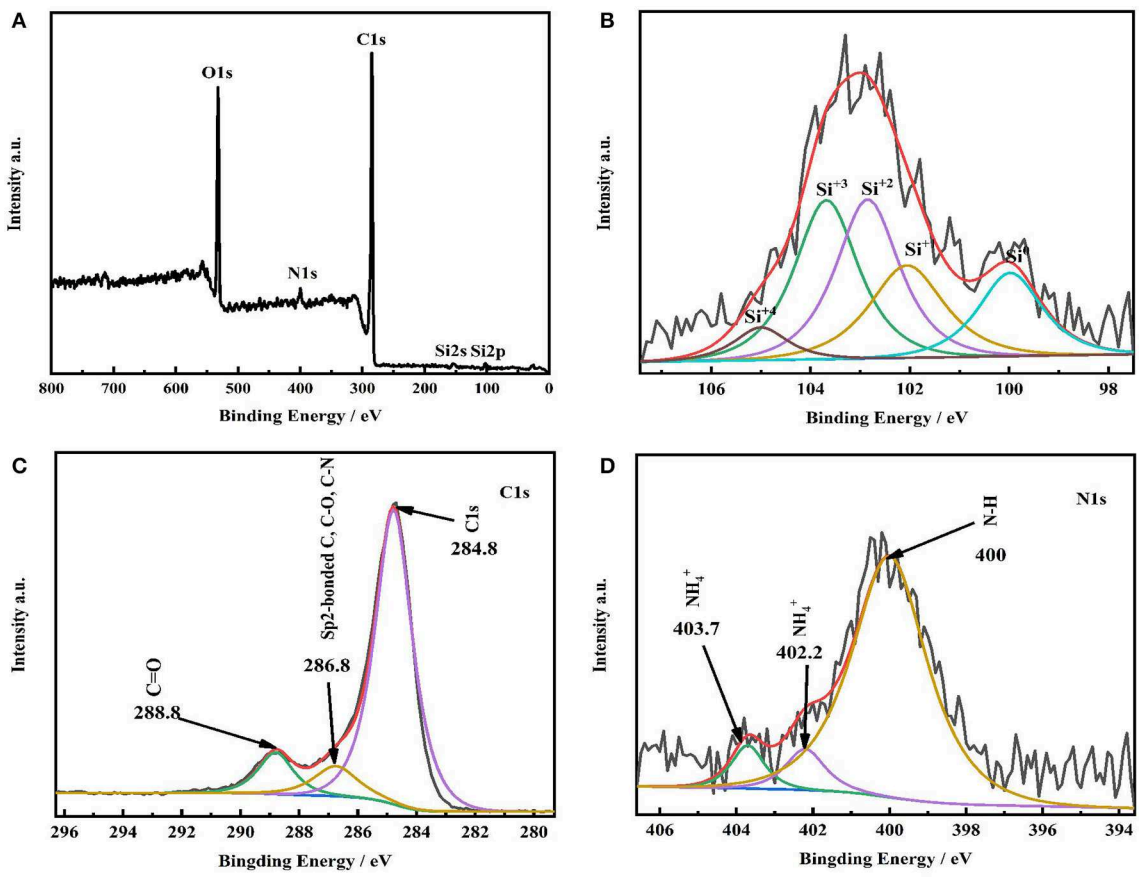

FIGURE 3 | (A–D) XPS spectra of SiO_x-G/PAA-PANi/graphene particles.

1,650 cm^{-1} belongs to the polyaniline. The two characteristic bands at 1,490 and 1,580 cm^{-1} are attributed to the stretching vibration of benzenoid C=C and the stretching vibration of quinonoid C=C, respectively. The band at 1,630 cm^{-1} can be assigned to N-H bending vibration (Li et al., 1999; Sivakkumar and Kim, 2007). The results confirm that the *in-suit* polymerization of PAA and aniline lead to the formation of PAA-PANi.

The element details of SiO_x-G/PAA-PANi/graphene were reflected by XPS. **Figure 3** shows the spectrum of all elements (**Figure 3A**), Si2p (**Figure 3B**), C1s (**Figure 3C**), and N1s (**Figure 3D**). The detail information about valence states of Si obtained from **Figure 3B** and described in **Table 1**. Clearly, the existence of Si^0(99.98 eV), Si^{1+}(102.06eV), Si^{2+}(102.85eV), Si^{3+}(103.68eV), and Si^{4+}(105.00eV) can be observed in the SiO_x-G/PAA-PANi/graphene sample, and the corresponding atomic percentages are 15.55, 20.11, 29.63, 29.63, and 5.08%, respectively (Zheng et al., 2018). The average valence of Si calculated from the Si 2p spectrum is 1.88. The XPS results of **Figure 3B** verifies the successful synthesis of SiO_x from the commercial SiO. The three peaks (Sp2-bonded C, C-O and C-N) deconvoluted from the C1s (**Figure 3C**) spectrum are situated at 286.75 eV, and C=O located at 288.8 eV. The bonding energy of C1s for graphite is located at 284.8 eV, indicating that graphite is present in SiO_x-G/PAA-PANi/graphene. It can be obtained from the N1s spectrum (**Figure 3D**) that there is a strong peak at 400.00 eV, being in correspondence with the characteristic chemical N-H of PANi. The protonated amines are located at 402.20 and 403.70 eV. N1s spectrum (**Figure 3D**) and FT-IR (**Figure 2**) images further confirmed the successful preparation of PAA-PANi by *in-situ* polymerization.

Figures 4a,b shows the SEM images of SiO_x-G/PAA-PANi/graphene. As clearly seen, graphene is distributed around SiO_x-G/PAA-PANi, which plays a supporting connection in the structure and can improve the conductivity. This results match with the results shown by the TEM (**Figures 4c,d**). **Figure 4c** shows the TEM image of SiO_x-G/PAA-PANi. As obtained from

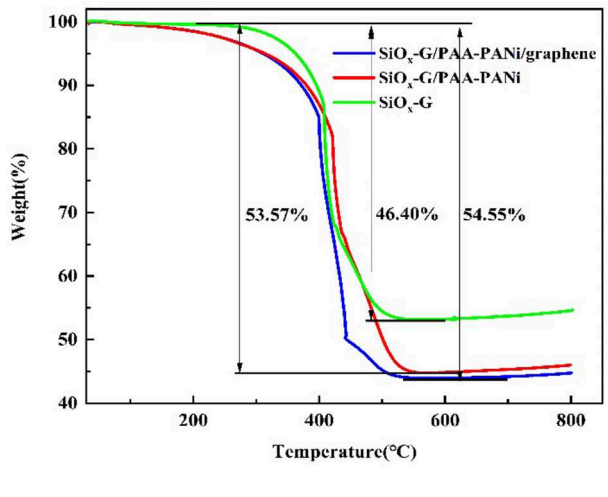

FIGURE 5 | TG image of SiO_x-G, SiO_x-G/PAA-PANi and SiO_x-G/PAA-PANi/graphene.

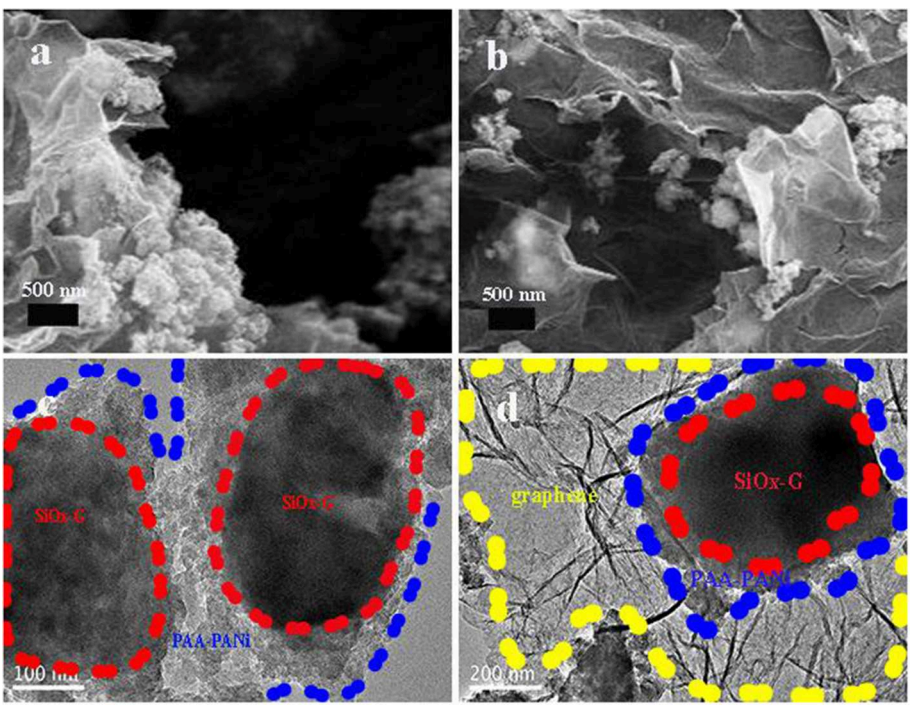

FIGURE 4 | (a,b) SEM images of SiO_x-G/PAA-PANi/graphene; **(c)** TEM image of SiO_x-G/PAA-PANi; **(d)** TEM image of SiO_x-G/PAA-PANi/graphene.

Figure 4a, the SiO_x-G particles are encapsulated inside the conductive hydrogel, and the coating thickness range of PAA-PANi ranges from 100 nm to 200 nm. **Figure 4d** depicts the TEM image of SiO_x-G/PAA-PANi/graphene. It can be observed that SiO_x-G/PAA-PANi particles are distributed between graphene.

The estimate of the carbon contents based on the three samples was obtained via TG measurement. The carbon contents of SiO_x-G, SiO_x-G/PAA-PANi, and SiO_x-G/PAA-PANi/graphene were about 46.85, 55.22, and 56.08 wt%, respectively (**Figure 5**). The superficial passivation of SiO_x lead to the oxidation of Si in air was not distinguished between 600 and 800°C (Chen et al., 2014; He et al., 2019; Jiang Y. et al., 2019; Jiang Z. et al., 2019). They are beneficial to improve the cycle performance of SiO to varying degrees.

Figure 6 displays the charge/discharge curves for SiO_x-G/PAA-PANi/graphene, SiO_x-G/PAA-PANi and SiO at a current density of 100 mA g^{-1}. The charge/discharge curves of the SiO electrode deliver a high initial discharge specific capacity of 2,156 mA h g^{-1} and an initial charge specific capacity of 1,165 mA h g^{-1} (ICE is 54%) and show a stable and obvious voltage platform around 0.1 V, in which the gentle slopes appears between 0.2 and 0.5 V. The first discharge-charge profiles of the SiO_x-G/PAA-PANi and SiO_x-G/PAA-PANi/graphene electrodes are similar to that of the Si-SiO_x-Cristobalite/Graphite electrode (Ren and Li, 2014). The first discharge and charge capacities of SiO_x-G/PAA-PANi composite are 1006.4 and 692.3 mA h g^{-1}, respectively, with an ICE of about 68.8%. The capacity of the first discharge and charge capacity of SiO_x-G/PAA-PANi/graphene is 1420.8 and 1062.3 mA h g^{-1}, respectively, with an ICE of about 74.77%. The large initial irreversible capacity is ascribed to the Li^+ consumption of to form the SEI film as well as the chemical reactions between Li and SiO_x.

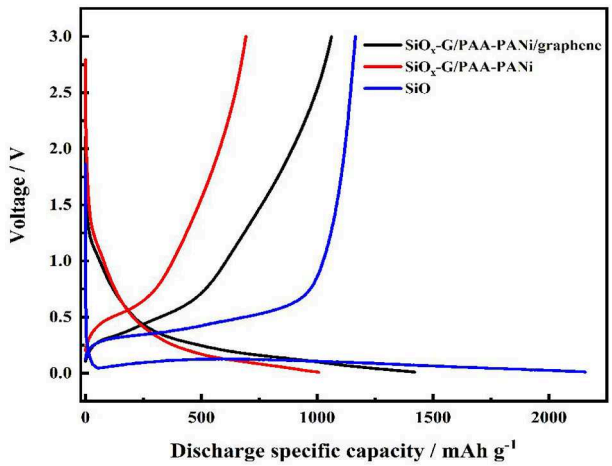

FIGURE 6 | The charge/discharge curves of SiO_x-G/PAA-PANi/graphene, SiO_x-G/PAA-PANi, and SiO anodes under the current density of 500 mA g^{-1}.

Figure 7A displays the cyclic voltammetry curves of the SiO_x-G/PAA-PANi. A relatively flat reduction peak appearing at 1.2 V and a strong reduction peak appearing at 0.65 V in the first lithiation process are corresponding to the decomposition of liquid electrolytes and formation of the SEI film, respectively (Ren and Li, 2014). The oxidation peak appearing at 0.18 V indicates that Li is detached from Li_xC, and the voltage position representing Li detached from Li_xSi is at 0.6 V in the first delithiation (Sivakkumar and Kim, 2007; Chen et al., 2014, 2018; Li et al., 2019). The reason for the incomplete reversibility of the electrode capacity is attributed to the by-products (Li_2O and $Li_2Si_2O_5$) formed by the irreversible chemical reactions between SiO_x and Li (Sivakkumar and Kim, 2007). There are two reduction peaks around 0.6 V and 0.2 V, which represent the lithiation process. **Figure 7B** shows the cyclic voltammetry curves of the SiO_x-G/PAA-PANi/graphene composite. Comparing with the CV curves of the SiO_x-G/PAA-PANi, there are the same reduction peaks around 0.6 and 0.2 V in the first cycle of SiO_x-G/PAA-PANi/graphene, which are attributed to lithium extraction from the SiO_x-G/PAA-PANi/graphene.

The rate performance of the SiO_x-G/PAA-PANi/graphene, SiO_x-G/PAA-PANi, and SiO electrodes is illustrated in **Figure 8**.

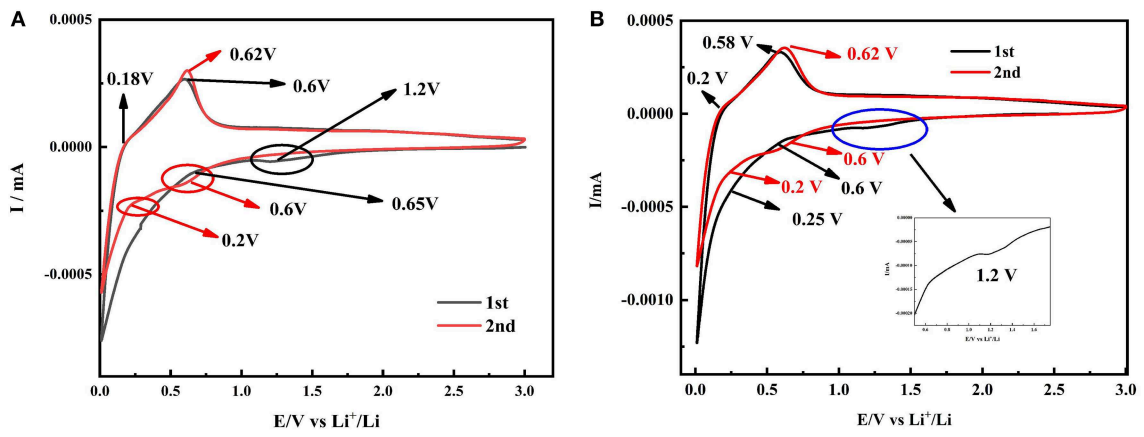

FIGURE 7 | CV curves of SiO_x-G/PAA-PANi **(A)** and SiO_x-G/PAA-PANi/graphene **(B)** electrodes at the scanning rate of 0.1 mV s^{-1}.

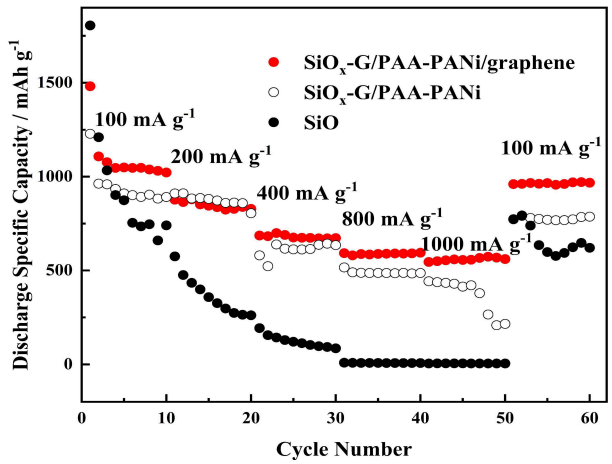

FIGURE 8 | The rate performances of SiO_x-G/PAA-PANi/graphene, SiO_x-G/PAA-PANi, and SiO electrodes.

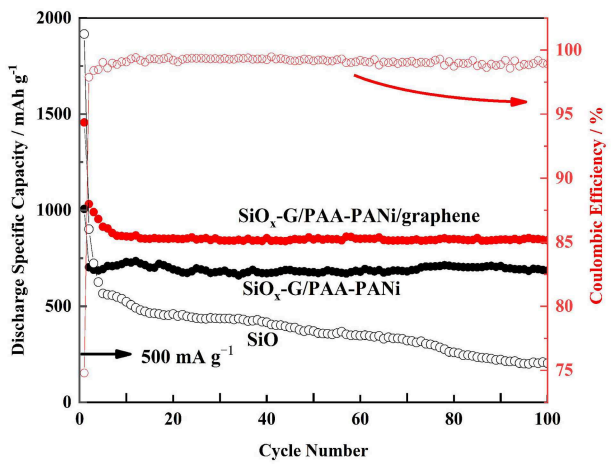

FIGURE 9 | Long-time cycling performances (discharge capacities) of SiO_x-G/PAA-PANi/graphene, SiO_x-G/PAA-PANi, and SiO under the current density of 500 mA g^{-1}.

The rate performance of the SiO electrode is significantly different from that of the SiO_x-G/PAA-PANi electrode, in which the rate performance of the SiO electrode is so unsatisfactory. Based on these results, the doping of conductive graphene further enhances the rate performance. The capacities of the SiO_x-G/PAA-PANi/graphene are 1022.3, 828.1, 675.7, 588.1, 556.2 mA h g^{-1} at a current density of 100, 200, 400, 800, and 1,000 mA g^{-1}, respectively. Moreover, the capacity can rise to 967.1 mA h g^{-1} as the current density returns to 100 mA g^{-1}, which demonstrates that SiO_x-G/PAA-PANi/graphene electrode can maintain a good structural stability.

Figure 9 indicates the cycling stability of SiO_x-G/PAA-PANi/graphene, SiO_x-G/PAA-PANi, and SiO electrodes at a current density of 500 mA g^{-1}. Although the initial discharge specific capacity of the SiO electrode reaches 1916.6 mA h g^{-1}, the capacity suddenly drops due to the rupture of the SiO structure. Compared with SiO, the cycle performance of SiO_x-G/PAA-PANi is significantly improved, and a high discharge specific capacity (685.4 mA h g^{-1}) is maintained when it is cycled to the 100th cycle, which can be attributed to the 3D structure of the conductive hydrogel that can serve as an effective buffer for the volume change of SiO_x nanoparticles. In contrast to SiO_x-G/PAA-PANi, SiO_x-G/PAA-PANi/graphene exhibits a significantly improved performance, with a discharge specific capacity of 842.3 mA h g^{-1} at current density of 500 mA g^{-1} at 100th cycle, and the coulombic efficiency is about 99% from 8th to 100th cycles, which is due to the improved electron transport.

CONCLUSIONS

In summary, the three-dimensional SiO_x-G/PAA-PANi/graphene hydrogel was prepared by a facile ball milling and *in-situ* polymerization process. The amorphous SiO_x-G was encapsulated within 3D mesh structure of PAA-PANi/graphene. According to the preparation method of the study, the specific capacity of SiO_x-G/PAA-PANi/graphene can be as high as 842.3 mA h g^{-1} at 500 mA g^{-1} when Li^+ are subjected to the 100th deintercalation, as well as the ICE is increased to 74.77% compared with SiO. The superior performance could be due to that PAA-PANi offers fast channels for electronic and ionic transfer and free space for SiO_x-G volume changes, and also the conductively active graphene effectively improves the electron transport.

DATA AVAILABILITY STATEMENT

The raw data supporting the conclusions of this article will be made available by the authors, without undue reservation, to any qualified researcher.

AUTHOR CONTRIBUTIONS

YR contributed conception, design of the study, and revised the manuscript. YL carried out experiments and wrote the manuscript. KL performed analyzed experimental results. XH revised the manuscript.

FUNDING

This work was financially supported by the National Nature Science Foundation of China (21576030 and U1607127).

REFERENCES

An, C., Yuan, Y., Zhang, B., Tang, L., Xiao, B., He, Z., et al. (2019). Graphene wrapped $FeSe_2$ nano-microspheres with high pseudocapacitive contribution for enhanced Na-ion storage. *Adv. Energy Mater.* 9:1900356. doi: 10.1002/aenm.201900356

Casimir, A., Zhang, H., Ogoke, O., Amine, J., Lu, J., and Wu, G. (2016). Silicon-based anodes for lithium-ion batteries: effectiveness of

materials synthesis and electrode preparation. *Nano Energy* 27, 359–376. doi: 10.1016/j.nanoen.2016.07.023

Chen, D., Yi, R., Chen, S., Xu, T., Gordin, M., and Wang, D. (2014). Facile synthesis of graphene–silicon nanocomposites with an advanced binder for high-performance lithium-ion battery anodes. *Solid State Ionics*. 254, 65–71. doi: 10.1016/j.ssi.2013.11.020

Chen, Y., Mao, Q., Bao, L., Yang, T., Lu, X., Du, N., et al. (2018). Rational design of coaxial MWCNTs@Si/SiO_x@C nanocomposites as extending-life anode materials for lithium-ion batteries. *Ceram. Int*. 44, 16660–16667. doi: 10.1016/j.ceramint.2018.06.093

Fang, R., Miao, C., Mou, H., and Xiao, W. (2019). Facile synthesis of Si@TiO_2@rGO composite with sandwich-like nanostructure as superior performance anodes for lithium ion batteries. *J. Alloys. Compd*. 818:152884. doi: 10.1016/j.jallcom.2019.152884

Han, X., Cui, X., Yi, T., Li, Y., and Yue, C. (2018). Recent progress of $NiCo_2O_4$-based anodes for high-performance lithium-ion batteries. *Curr. Opin. Solid State Mater Sci*. 22, 109–126. doi: 10.1016/j.cossms.2018.05.005

He, X., Sun, Z., Zou, Q., Yang, J., and Wu, L. (2019). Codeposition of nanocrystalline Co-Ni catalyst based on 1-ethyl-3-methylimidazolium bisulfate and ethylene glycol system for hydrogen evolution reaction. *J. Electrochem. Soc*. 166, D908–D915. doi: 10.1149/2.0171916jes

Huang, X., Yin, Z., Wu, S., Qi, X., He, Q., Zhang, Q., et al. (2011). Graphene-based materials: synthesis, characterization, properties, and applications. *Small* 7, 1876–1902. doi: 10.1002/smll.201002009

Hwa, Y., Park, C., and Sohn, H. (2013). Modified SiO as a high performance anode for Li-ion batteries. *J. Power Sour*. 22, 129–134. doi: 10.1016/j.jpowsour.2012.08.060

Jiang, B., Zeng, S., Wang, H., Liu, D., Qian, J., Cao, Y., et al. (2016). Dual core–shell structured Si@SiO_x@C nanocomposite synthesized via a one-step pyrolysis method as a highly stable anode material for lithium-ion batteries. *Appl. Mater. Interfaces* 8, 31611–31616. doi: 10.1021/acsami.6b09775

Jiang, Y., Feng, X., Cheng, G., Li, Y., Li, C., He, Z., et al. (2019). Electrocatalytic activity of MnO_2 nanosheet array-decorated carbon paper as superior negative electrode for vanadium redox flflow Batteries. *Electrochim. Acta*. 322:134754. doi: 10.1016/j.electacta.2019.134754

Jiang, Z., Li, Y., Zhu, J., Li, B., Li, C., Wang, L., et al. (2019). Synthesis and performance of a graphene decorated $NaTi_2(PO_4)_3$/C anode for aqueous lithium-ion batteries. *Alloys J. Compd*. 791, 176–183. doi: 10.1016/j.jallcom.2019.03.289

Li, C., Bai, H., and Shi, G. (2009). Conducting polymer nanomaterials: electrosynthesis and applications. *Chem. Soc. Rev*. 38, 2397–2409. doi: 10.1039/b816681c

Li, D., Jiang, Y., Li, C., Wu, Z., Chen, X., and Li, Y. (1999). Self-assembly of polyaniline/polyacrylic acid films via acid–base reaction induced deposition. *Polymer* 40, 7065–7070. doi: 10.1016/S0032-3861(99)00118-4

Li, J., Zhang, G., Yang, Y., Yao, D., Lei, Z., Li, S., et al. (2018). Glycinamide modified polyacrylic acid as high-performance binder for silicon anodes in lithium-ion batteries. *Power Sour. J*. 406, 102–109. doi: 10.1016/j.jpowsour.2018.10.057

Li, P., Jin, Z., Peng, L., Zhao, F., Xiao, D., Jin, Y., et al. (2018). Stretchable all-gel-state fiber-shaped supercapacitors enabled by macromolecularly interconnected 3D graphene/nanostructured conductive polymer hydrogels. *Adv. Mater*.20181800124. doi: 10.1002/adma.201800124

Li, R., Xiao, W., Miao, C., Fang, R., Wang, Z., and Zhang, M. (2019). Sphere-like SnO_2/TiO_2 composites as high-performance anodes for lithium ion batteries. *Ceram. Int*. 45, 13530–13535. doi: 10.1016/j.ceramint.2019.04.059

Liu, D., Fan, X., Li, Z., Liu, T., Ling, M., Liu, Y., et al. (2019). A cation/anion co-doped $Li_{1.12}Na_{0.08}Ni_{0.2}Mn_{0.6}O_{1.95}F_{0.05}$ cathode for lithium ion batteries. *Nano Energy* 58, 786–796. doi: 10.1016/j.nanoen.2019.01.080

Liu, Y., Fan, X., Zhang, Z., Wu, H., Liu, D., Dou, A., et al. (2019b). Enhanced electrochemical performance of Li-rich layered cathode materials by combined Cr doping and $LiAlO_2$ coating. *ACS Sustainable Chem. Eng*. 7, 2225–2235. doi: 10.1021/acssuschemeng.8b04905

Liu, Y., Tang, L., Wei, H., Zhang, X., He, Z., Li, Y., et al. (2019a). Enhancement on structural stability of Ni-Rich cathode materials by *in-situ* fabricating dual-modified layer for lithium-ion batteries. *Nano Energy* 65:104043. doi: 10.1016/j.nanoen.2019.104043

Nguyen, D., Nguyen, C., Kim, J., Kim, J., and Song, S. (2013). Facile synthesis and high anode performance of carbon fiber-interwoven amorphous nano-SiO_x/graphene for rechargeable lithium batteries. *ACS Appl. Mater. Interfaces* 5, 11234–11239. doi: 10.1021/am4034763

Qian, L., Lan, J., Xue, M., Yu, Y., and Yang, X. (2017). Two-step ball-milling synthesis of a Si/SiO_x/C composite electrode for lithium ion batteries with excellent long-term cycling stability. *RSC Adv*. 7, 36697–36704. doi: 10.1039/C7RA06671F

Ren, Y., and Li, M. (2014). Si-SiO_x-cristobalite/graphite composite as anode for Li-ion batteries. *Electrochim. Acta*. 142, 11–17. doi: 10.1016/j.electacta.2014.07.101

Sivakkumar, S., and Kim, D. (2007). Polyaniline/carbon nanotube composite cathode for rechargeable lithium polymer batteries assembled with gel polymer electrolyte. *J. Electrochem. Soc*. 54:A134. doi: 10.1149/1.2404901

Wang, K., Huang, X., Zhou, T., Wang, H., Xie, H., and Ren, Y. (2020). Boosted electrochemical properties of porous Li_2FeSiO_4/C based on Fe-MOFs precursor for lithium ion batteries. *Vacuum*. 171:108997. doi: 10.1016/j.vacuum.2019.108997

Wang, L., Zhang, P., Su, L., and Ma, C. (2014). SiO_x-PANI-Ag composites with Homogeneously-embedded Si nanocrystals and nanopores as high-performance anodes for lithium ion batteries. *J. Mater. Chem. A* 2, 3776–3782. doi: 10.1039/c3ta14498d

Wang, Y., Wang, X., Tang, S., and Vongehr, S. (2015). Highly processible and electrochemically active graphene-doped polyacrylic acid/polyaniline allowing the preparation of defect-free thin films for solid-state supercapacitors. *RSC Adv*. 5, 62670–62677. doi: 10.1039/C5RA05486A

Wu, H., Yu, G., Pan, L., Liu, N., McDowell, M., Bao, Z., et al. (2013). Stable Li-ion battery anodes by *in-situ* polymerization of conducting hydrogel to conformally coat silicon nanoparticles. *Nat. Commun*. 4:1943. doi: 10.1038/ncomms2941

Xiao, B., Wang, P., Zhang, B., He, Z., Yang, Z., Tang, L., et al. (2019). Effect of MgO and TiO_2 coating on electrochemical performance of Li-Rich cathode materials for lithium-ion batteries. *Energy Technol*. 7:1800829. doi: 10.1002/ente.201800829

Xiao, W., Wang, Z., Zhang, Y., Fang, R., Yuan, Z., Miao, C., et al. (2018). Enhanced performance of P(VDF-HFP)-based composite polymer electrolytes doped with organic-inorganic hybrid particles PMMA-ZrO_2 for lithium ion batteries. *J. Power Sour*. 382, 128–134. doi: 10.1016/j.jpowsour.2018.02.012

Xu, Q., Sun, J., Yin, Y., and Yu, G. (2017). Facile synthesis of blocky SiO_x/C with graphite-like structure for high-performance lithium-ion battery anodes. *Adv. Funct. Mater*.28:1705235. doi: 10.1002/adfm.201705235

Xu, Q., Sun, J., Yu, Z., Yin, Y., Xin, S., Yu, S., et al. (2018). SiO_x encapsulated in graphene bubble film: an ultrastable Li-on battery anode. *Adv. Mater*. 30:1707430. doi: 10.1002/adma.201707430

Yang, S., Wang, P., Wei, H., Tang, L., Zhang, X., He, Z., et al. (2019). $Li_4V_2Mn(PO_4)_4$-stablized $Li[Li_{0.2}Mn_{0.54}Ni_{0.13}Co_{0.13}]O_2$ cathode materials for lithium ion batteries. *Nano Energy* 63:103889. doi: 10.1016/j.nanoen.2019.103889

Yi, T., Peng, P., Fang, Z., Zhu, Y., Xie, Y., and Luo, S. (2019). Carbon-coated $LiMn_{1-x}Fe_xPO_4$ ($0 \leq x \leq 0.5$) nanocomposites as high-performance cathode materials for Li-ion battery. *Compos. Part B*. 175:107067. doi: 10.1016/j.compositesb.2019.107067

Yi, T., Zhu, Y., Tao, W., Luo, S., Xie, Y., and Li, X. (2018). Recent advances in the research of $MLi_2Ti_6O_{14}$ (M=2Na, Sr, Ba, Pb) anode materials for Li-ion batteries. *J. Power Sour*. 339, 26–41. doi: 10.1016/j.jpowsour.2018.07.086

Yu, B., Hwa, Y., Park, C., and Sohn, H. (2013). Reaction mechanism and enhancement of cyclability of SiO anodes by surface etching with NaOH for Li-ion batteries. *J. Mater. Chem. A*. 1:4820. doi: 10.1039/c3ta00045a

Yu, Q., Ge, P., Liu, Z., Xu, M., Yang, W., Zhou, L., et al. (2018). Ultrafine SiO_x/C nanospheres and their pomegranate-like assemblies for high performance lithium storage. *J. Mater. Chem. A* 10:1039. doi: 10.1039/C8TA03987A

Zhao, L., Dvorak, D., and Obrovac, M. (2016). Layered amorphous silicon as negative electrodes in lithium-ion batteries. *J. Power Sour*. 332, 290–298. doi: 10.1016/j.jpowsour.2016.09.124

Zheng, J., Yang, Z., He, Z., Tong, H., Yu, W., and Zhang, J. (2018). *In situ* formed $LiNi_{0.8}Co_{0.15}Al_{0.05}O_2$@$Li_4SiO_4$ composite cathode material with high rate capability and long cycling stability for lithium-ion batteries. *Nano Energy* 53, 613–621. doi: 10.1016/j.nanoen.2018.09.014

Zheng, S., Dou, A., Su, M., and Liu, Y. (2020). Influence of Nb doping on electrochemical performance of nanostructured cation disordered

$Li_{1+x/100}Ni_{1/2-x/100}Ti_{1/2-x/100}Nb_{x/100}O_2$ composites cathode for Li-ion batteries. *J. Nanosci. Nanotechnol.* 20, 452–459. doi: 10.1166/jnn.2020.16884

Zheng, S., Liu, D., Tao, L., Fan, X., Liu, K., Liang, G., et al. (2019). Electrochemistry and redox characterization of rock-salt-type lithium metal oxides $Li_{1+z/3}Ni_{1/2-z/2}Ti_{1/2+z/6}O_2$ for Li-ion batteries. *Alloys J. Compd.* 773, 1–10. doi: 10.1016/j.jallcom.2018.09.261

Zhou, C., Wang, P., Zhang, B., Tang, L., and Tong, H., He, Z., et al. (2019). Formation and effect of residual lithium compounds on Li-rich cathode material $Li_{1.35}[Ni_{0.35}Mn_{0.65}]O_2$. *ACS Appl. Mater. Interfaces* 11, 11518–11523. doi: 10.1021/acsami.9b01806

Zhu, L., Du, F., Zhuang, Y., Dai, H., Cao, H., Adkins, J., et al. (2019). Effect of crosslinking binders on Li-storage behavior of silicon particles as anodes for lithium ion batteries. *J. Electroanal. Chem.* 845, 22–30. doi: 10.1016/j.jelechem.2019.05.019

Zuo, D., Song, S., An, C., Tang, L., He, Z., and Zheng, J. (2019). Synthesis of sandwich-likestructured Sn/SnO_x@MXene composite through *in-situ* growth for highly reversible lithium storage. *Nano Energy* 62, 401–409. doi: 10.1016/j.nanoen.2019.05.062

Zuo, X., Zhu, J., Müller-Buschbaum, P., and Cheng, Y. (2017). Silicon based lithium-ion battery anodes: a chronicle perspective review. *Nano Energy* 31, 113–143. doi: 10.1016/j.nanoen.2016.11.013

Conflict of Interest: The authors declare that the research was conducted in the absence of any commercial or financial relationships that could be construed as a potential conflict of interest.